Materials Science and Engineering: A 588 (2013),pp. 7–13
DOI: http://dx.doi.org/10.1016/j.msea.2013.08.044

Anisotropy of uni-axial and bi-axial deformation behavior of pure Titanium after hydrostatic extrusion

E.C. Moreno-Valle [a,*], W. Pachla [b], M. Kulczyk [b], B. Savoini [c], M.A. Monge [c], C. Ballesteros [c], I. Sabirov [a]

[a] IMDEA Materials Institute, Calle Eric Kandel 2, Getafe 28906, Madrid, Spain
[b] Institute of High Pressure Physics, Polish Academy of Sciences (Unipress), ul. Sokolowska 29, 01-142 Warsaw, Poland
[c] Departamento de Física, Universidad Carlos III de Madrid, Av. Universidad 30, 28911 Madrid, Spain

Abstract: Coarse-grained commercially pure (CP) Titanium is subjected to hydrostatic extrusion resulting in the formation of ultrafine lamellar-type microstructure having very strong fiber texture. Uni-axial tensile tests of longitudinal and transverse specimens are carried out to study anisotropy of uni-axial deformation behavior of hydrostatically extruded CP Titanium. Small punch testing of longitudinal and transverse specimens is performed to study the anisotropy of its bi-axial deformation behavior. It is demonstrated that there is significant anisotropy of both uni-axial and bi-axial deformation of CP Titanium after hydrostatic extrusion which is related to the specific microstructure and texture developed in the material during hydrostatic extrusion.

Keywords: Titanium, Hydrostatic extrusion, Texture, Uni-axial deformation behavior Bi-axial deformation behavior Anisotropy

1. Introduction

Commercially pure (CP) Ti has been widely used in various sectors of engineering including biomedical industry due to its high corrosion resistance and good biocompatibility [1]. However, CP Ti has relatively low mechanical strength limiting its application [1]. Alloying can significantly enhance mechanical performance of CP Ti, but some alloying elements such as vanadium increase the toxicity and degrade its corrosion properties [2]. Nowadays, development of severe plastic deformation (SPD) techniques [3] has enabled formation of ultrafine-grained (UFG) microstructure in CP Ti leading to its enhanced mechanical strength. These SPD methods include equal-channel angular pressing (ECAP) [4,5], ECAP in combination with extrusion (or rolling, swaging, drawing) [6–8], high pressure torsion (HPT) [9,10], cryo-rolling followed by annealing [11], cross rolling [12,13], etc. Hydrostatic extrusion appears as one of the most promising SPD methods for fabrication of UFG CP Ti since it has some advantages [14]. First, very long rods can be processed via hydrostatic extrusion and, second, the method has a very high efficiency due to the very high processing strain rates, usually $> 10\,s^{-1}$ but can exceed $10^4\,s^{-1}$. A body of research on the microstructure and mechanical properties of pure Ti after hydrostatic extrusion exists in the literature [15–18]. It was demonstrated that grain size can be successfully refined down to the nanoscale if a strain of 5.47 is induced into rods during hydrostatic extrusion, leading to a mechanical yield strength of 1245 MPa in the longitudinal direction [15]. The effect of hydrostatic extrusion temperature (in the temperature range of 20–450 °C) on the microstructure, texture and mechanical properties of CP Ti was analyzed in [17]. It was shown that extrusion at room temperature leads to formation of a lamellar-type microstructure with the width of lamellae in the range of 100–500 nm, whereas extrusion at 300–450 °C results in formation of a bi-modal microstructure consisting of packs of lamellae and ultrafine grains. Significant increase of mechanical strength was observed after hydrostatic extrusion at all temperatures. As is well known, being hcp metal, α-Ti can show significant anisotropy of mechanical properties depending on the texture developed during materials processing [7,19]. However, no detailed studies on the anisotropy of mechanical properties in the hydrostatically extruded Ti rods have been performed yet. Fundamental understanding of the effect of hydrostatic extrusion on the anisotropy of mechanical behavior of pure Ti is necessary in order to predict the performance of the final engineering components.

The objective of the present work is to study the effect of hydrostatic extrusion on the microstructure, texture, and mechanical properties of pure Ti with greater respect to the anisotropy of uni-axial and bi-axial deformation behavior in the processed material. In most

* Corresponding author. Tel.: +34 91 549 34 22; fax: +34 91 550 30 47.
E-mail address: eva.moreno@imdea.org (E.C. Moreno-Valle).

Table 1
Parameters of hydrostatic extrusion applied to CP Ti (Grade 3).

Number of extrusion steps	Total cumulative reduction ratio, R_{cum}	Total cumulative true strain, ε_{cum}	Extrusion pressure [MPa]	Linear extrusion speed [mm/s]	Strain rate [s^{-1}]	Adiabatic heating, ΔT [°C]
4	25.41	3.24	630–1050	24–60	6–10	240–400

of metalforming operations, material is deformed in multi-axial mode along complex strain path [20]. Therefore, understanding of anisotropy of bi-axial deformation behavior of the extruded Ti is necessary if metalforming operations will be required for fabrication of complex shape parts from extruded Ti. It should be noted that research on bi-axial deformation behavior of SPD processed metals is very limited [21–23] and anisotropy of bi-axial deformation behavior of the SPD processed metals has not been studied yet.

2. Material and processing

CP Ti (Grade 3) with specification corresponding to the ASTM B348-09 standard [24] was supplied in the form of bars having a diameter of 50 mm. The as-received bar was subjected to hydrostatic extrusion at room temperature in four extrusion steps to the cumulative strain of 3.24 using a 45° die. Detailed description of hydrostatic extrusion process can be found in [25]. The strain rate at the last extrusion step was 10 s^{-1} which corresponds to the linear extrusion speed above 60 mm/s. Different combinations of lubricant paste based on ~60% MoS and refined oil, copper and PTFE aerosols, an aluminum layer deposited by physical vapor deposition (PVD) were tried as lubricants. The parameters of hydrostatic extrusion are outlined in Table 1. The rods after hydrostatic extrusion showed smooth surface without any (micro)cracks.

Hydrostatic extrusion is usually accompanied by significant adiabatic heating which might significantly affect the microstructure developed during processing [25]. The temperature rise due to adiabatic heating was estimated by the commonly accepted equation [25–27],

$$\Delta T = \beta \frac{W}{c\rho} = \beta \frac{p}{c\rho} \quad (1)$$

where W is the plastic deformation work per unit volume, c the specific heat, ρ the material density, p the extrusion pressure, and the dimensionless parameter β denotes the fraction of plastic work converted into heat during deformation. For hydrostatic extrusion with a good insulation by a lubrication layer around the work-piece and high extrusion speed, β is taken as 0.9 [25]. For $c = 0.523$ J g^{-1} K^{-1} and $\rho = 4.5$ g cm^{-3}, Eq. (1) gives a temperature increase, ΔT, in the range of 240–400 °C.

3. Experimental procedures

The specimens for light optical microscopy studies were cut from the extruded rods on the longitudinal L-section (parallel to the rod axis/extrusion direction) and transverse T-section (perpendicular to the rod axis/extrusion direction), as shown in Fig. 1. The specimens were grinded and polished to mirror-like surface using standard metallographic technique. The final step was a chemical–mechanical polishing with a mixture of colloidal silica oxide polishing suspension (OPS) and 5% vol of H_2O_2. Optical microscopes Nikon Eclipse LV150 and OLYMPUS BX 51 were employed for the microstructural analysis.

The specimens for transmission electron microscopy (TEM) studies were cut from the L- and T-sections of the processed rods. The specimens were thinned by electropolishing in a TENUPOL 5 twin-jet polisher using a 1:4 solution of nitric acid in methanol at $T \sim -30$ °C. The TEM analyses were carried out in a TECNAI-20-FEG microscope operated at 200 kV equipped with an X-ray energy dispersive spectrometer. For Z-contrast measurements, a scanning transmission electron microscopy (STEM) modulus with a dark-field high angle annular detector (HAADF) was employed. Selected area electron diffraction (SAED) patterns were recorded from the areas of interest.

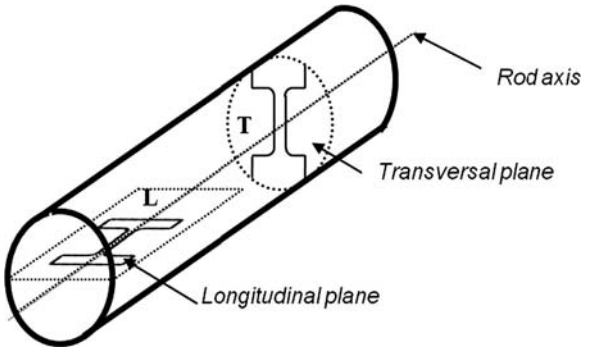

Fig. 1. Rod axis, longitudinal and transverse planes and orientation of specimens in the extruded rod.

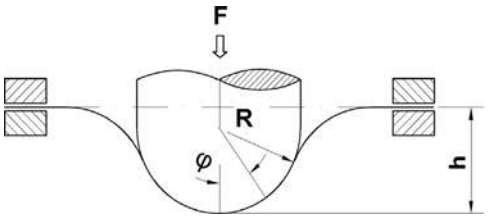

Fig. 2. Schematic drawing of small punch testing.

Texture measurements were performed at the CAI DRX at the Complutense University of Madrid using a Phillips Xpert'PRO diffractometer equipped with a PW3050/60 goniometer. Measurements were taken in a range of Φ angles from 0° to 75° at 3° steps. The pole figures for the planes (0001), (10 − 10), (10 − 11), (10 − 12), (10 − 13), and (10 − 20) were plotted.

To study uni-axial tensile behavior of the material, specimens for tensile testing were cut from the extruded rods so their tensile axis was perpendicular to the rod axis (T-specimens) and parallel to the rod axis (L-specimens), as shown in Fig. 1. Tensile specimens of gauge length 3.2 mm and gauge width of 0.8 mm were mechanically polished to mirror-like surface using colloidal silica solution at the final stage. Tensile tests were carried out at room temperature using the universal tensile/compression module 'Kammrath&Weiss'. Tensile specimens were deformed to failure with constant cross-head speed corresponding to the initial strain rate of 10^{-3} s^{-1}. The mechanical properties (0.2% proof strength $\sigma_{0.2}$, ultimate tensile strength, σ_{UTS}, uniform elongation, ε_u, and elongation to failure, ε_f) were determined from the obtained engineering stress–strain curves. At least three specimens were tested for each condition and the results were reproducible.

To study bi-axial deformation behavior of the material, flat specimens for small punch testing were cut in the T- and L-sections of the extruded rods (Fig. 1). Both sides of the flat

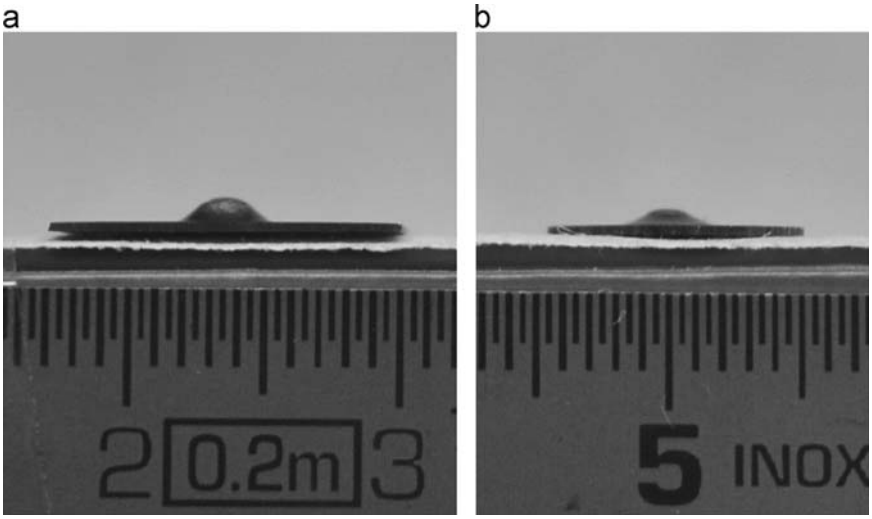

Fig. 3. Appearance of specimens after small punch testing of CP Ti: (a) as-received T-specimen and (b) hydrostatically extruded T-specimen.

specimens were grinded and polished to mirror-like surfaces using colloidal silica at the final stage. The final thickness of specimens was 0.4 mm. A schematic diagram of a small punch testing is illustrated in Fig. 2. A flat punch specimen is clamped between upper and bottom dies. It is deformed at room temperature by a well lubricated hemi-spherical rigid punch having a diameter of 2.4 mm. The die design is similar to that widely used for small punch testing [28–33]. Punch speed during testing was 0.5 mm/min. Load F and central deflection h readings were taken during testing (Fig. 2). Small punch tests were stopped at the moment of onset of plastic instability on the load–central deflection curve. Fig. 3 illustrates appearance of specimens after small punch testing. It is clearly seen that specimens are deformed into a dome shaped cap. To estimate the equivalent strain induced in these small punch specimens, final thickness was measured over areas deformed under membrane (bi-axial) stretching. The true strain was estimated as

$$\varepsilon = \ln\left(\frac{t_0}{t}\right) \tag{2}$$

where t_0 is the initial thickness and t the final thickness of the small punch specimen. At least three specimens were tested per each condition and the results were found to be reproducible.

Qualitative examination of surface relief after deformation of small punch specimens was performed using an EVO MA 15 SEM operating at 20 kV. Surface relief was analyzed in the area of bi-axial stretching.

4. Results and discussions

4.1. Effect of hydrostatic extrusion on microstructure and texture of CP Ti

Optical microscopy images of the as-received CP Titanium are presented in Fig. 4a. A homogeneous microstructure consisting of equiaxed grains having the average size of 42 μm is observed. Fig. 4b shows a representative optical micrograph of a longitudinal section of the CP Titanium samples after hydrostatic extrusion. It is seen that hydrostatic extrusion led to fragmentation and elongation of grains along extrusion direction resulting in the complex microstructure which cannot be clearly resolved with light optical microscope. TEM examination of the samples showed that hydrostatic extrusion leads to a microstructure consisting of lamellae aligned along the extrusion axis and having a length up to 1 μm

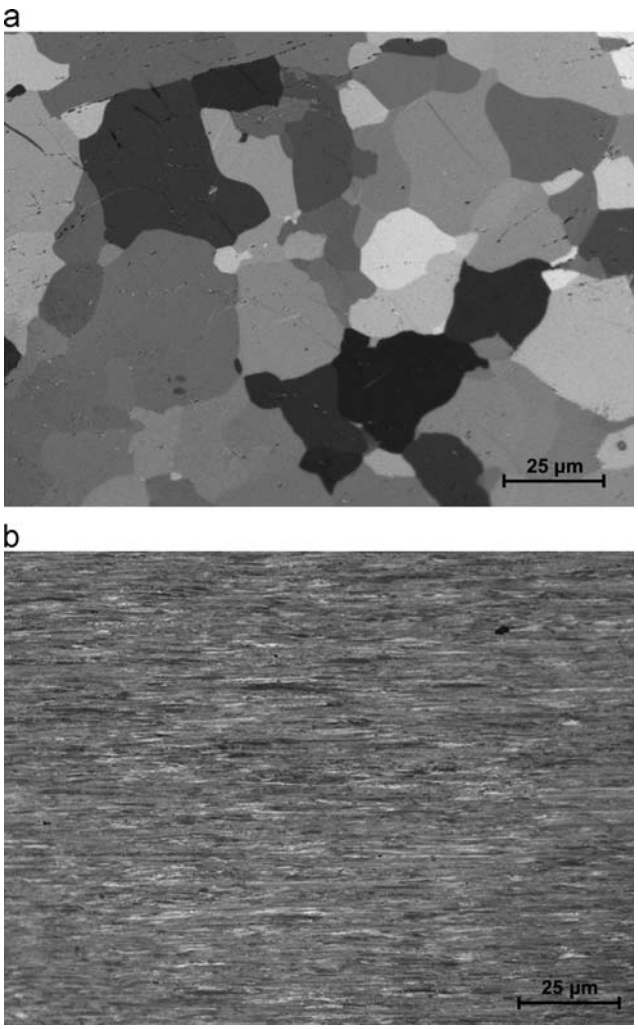

Fig. 4. Optical images of microstructure of CP Ti: (a) as-received; (b) hydrostatically extruded (L plane). Extrusion direction is horizontal.

and a width ranging from 10 to 100 nm (Fig. 5a). A high density of dislocations is observed in the lamellae interior and the formation of equiaxed grains/subgrains is also seen (Fig. 5b). They present straight boundaries intersecting at high angles with neighbor

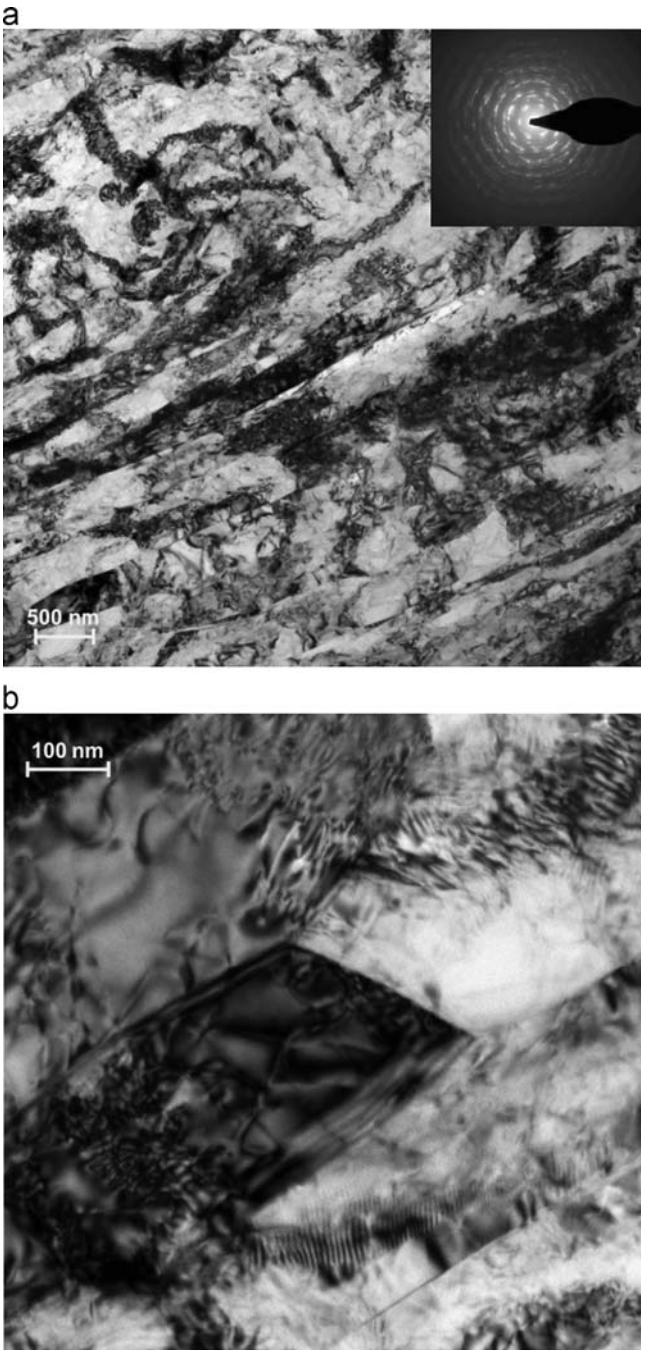

Fig. 5. TEM images of the microstructure of CP Ti after hydrostatic extrusion (L plane).

lamellae. The formation of this microstructure can be related explicitly to twinning and dislocation glide operating in the material during hydrostatic extrusion. Despite hydrostatic extrusion results in significant adiabatic heating of metallic materials [25], the temperature of adiabatic heating in our hydrostatically extruded pure Ti estimated using Eq. (1) (Table 1) is well below the recrystallization temperatures of 620–760 °C reported for severely deformed pure Ti [35,36]. Moreover, it should be noted that the samples during hydrostatic extrusion are heated only in the local deformed volume within the die work-piece during milliseconds and they are immediately cooled down (water quenched) to room temperature, that is insufficient in case of CP Titanium neither for recrystallization nor for significant recovery of the developed microstructure [34,35].

Fig. 6 illustrates pole figures for the T-section of pure Ti before and after hydrostatic extrusion. The as-received material shows a weak texture somewhat similar to that demonstrated by hot rolled pure Ti (Fig. 6a) [36]. Hydrostatic extrusion breaks up the initial texture and leads to formation of very strong fiber texture with $\langle 10\bar{1}0 \rangle$ direction parallel to the rod axis and basal planes (0001) parallel to the rod axis (Fig. 6b). The maximum intensity on the $(10\bar{1}0)$ pole figure increases up to ~17. Such fiber texture is typical for CP Ti subjected to conventional extrusion, drawing or swaging [37].

4.2. Effect of hydrostatic extrusion on mechanical behavior and its anisotropy

4.2.1. Uni-axial tensile behavior and its anisotropy

Fig. 7 shows the engineering stress–strain curves from tensile tests at room temperature in the L- and T-directions of the as-received and hydrostatically extruded CP Ti. Mechanical properties are listed in Table 2. A slight anisotropy of mechanical properties is observed in the as-received CP Titanium. The T-specimens tend to show higher mechanical properties compared to the L-specimens (Fig. 7, Table 2) due to the weak crystallographic texture present in the as-received material (Fig. 6a). No significant effect of the sample orientation on the work hardening capacity defined as $\sigma_{UTS}/\sigma_{0.2}$ is observed (Fig. 7). The mechanical strength of CP Ti dramatically increases after hydrostatic extrusion due to grain refinement whereas both uniform elongation and elongation to failure show an opposite trend (Table 2). Significant anisotropy of uni-axial tensile mechanical behavior is observed. The L-specimens display very high $\sigma_{0.2}$-value, 915 MPa, but low work hardening capacity, so the σ_{UTS}-value of the material is 970 MPa (Fig. 7, Table 2). On the other hand, the T-specimens show a much lower $\sigma_{0.2}$-value, 562 MPa, but a similar σ_{UTS}-value, 995 MPa, indicating a very high work hardening capacity of the T-specimens (Fig. 7, Table 2). This anisotropy of mechanical behavior can be rationalized based on the very strong crystal-lographic macrotexture developed in the material during hydro-static extrusion (Fig. 6b) [7,19]. It is well known that dislocation glide and twinning are the main mechanisms operating during plastic deformation of CP Ti at room temperature [37,38]. Defor-mation twinning is suppressed in the UFG CP Ti [38,39]. The main dislocation slip modes in CP Ti at room temperature having the lowest critical resolved shear stresses are the prismatic $\langle 11\bar{2}0 \rangle \{10\bar{1}0\}$ slip system and the basal $\langle 11\bar{2}0 \rangle \{0001\}$ slip system [38,40]. Additionally, dislocation glide on pyramidal systems $\langle 11\bar{2}0 \rangle \{10\bar{1}1\}$ and $\langle 11\bar{2}3 \rangle \{10\bar{1}1\}$ can be also activated [40]. The operating systems are generally determined by the Von Misses criterion, the Schmid factors, and the critical resolved shear stress. In the L-specimens, basal planes are suppressed since they are parallel to the tensile axis and two of the prismatic slip planes are suppressed since they are perpendicular to the tensile axis. The remaining four prismatic slip planes are inclined at 60° to the tensile axis and can be active. So, the high yield strength of the material can be related to the limited number of prismatic slip systems available. In the T-specimens, the *c*-axis of the h.c.p. lattice of individual grains is randomly inclined with respect to the tensile axis. Thus, the microstructure will be formed by a combi-nation of soft and hard grains, depending on the individual orientations. The grains that are most favorably oriented for prismatic and basal slip can be easily deformed at lower values of applied stress (soft grains). Localization of plastic slip within these grains results in local strain hardening, and, in turn, in an increase of the flow stress, and in the spread of plastic slip to grains that are less favorably oriented for prismatic and basal slip. This scenario leads to overall high work hardening capacity of the T-specimens. It should be also noted that a higher work hardening

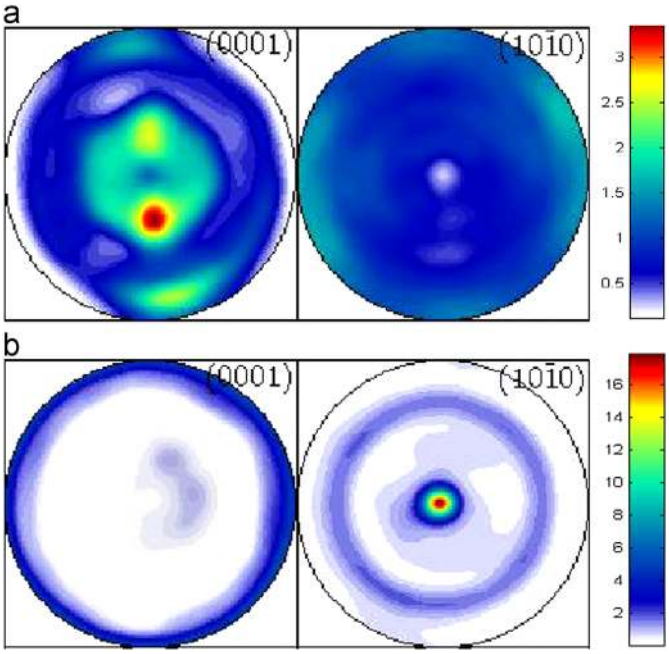

Fig. 6. Pole figures for CP Ti: (a) in the as-received condition; (b) after hydrostatic extrusion. Scale represents multiples of random distribution (mrd).

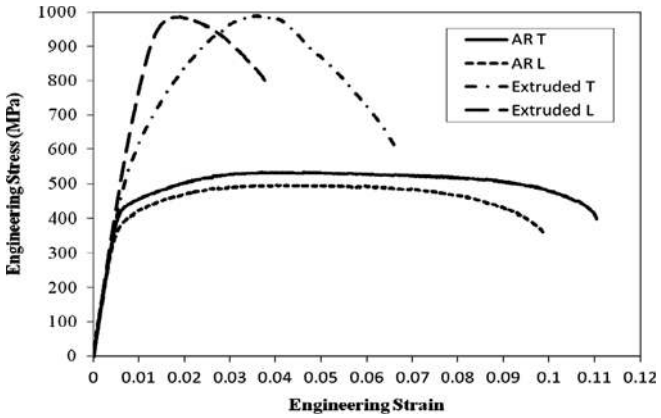

Fig. 7. Engineering stress–strain curves from tensile testing of CP Ti in the as-received (AR) condition and after hydrostatic extrusion.

ability of these T-specimens delays macro-localization of plastic flow resulting in higher uniform elongation (~2.7%) and higher elongation to failure (~6%) compared to those for the L-specimens (~0.9% and ~3.1%) according to the well-known Considere criterion [41].

4.2.2. *Bi-axial deformation behavior and its anisotropy*

Load–central deflection curves from small punch testing of the as-received and extruded CP Ti are presented in Fig. 8. Typical stages of formability behavior are marked on the curve for the as-received specimens. The first stage corresponds to elastic bending that is associated with local surface micro-yielding. During the second stage, plastic bending, plastic flow begins and spreads within the specimen-punch contact zone. Bi-axial deformation of flat specimen into dome shaped cap occurs during the next stage, membrane stretching [42]. Once maximum load capacity is reached, unstable plastic flow begins resulting in the formation of cracks and specimen failure. The results of small punch testing are listed in Table 3. No any anisotropy of bi-axial deformation behavior is observed in the as-received material, since the load-central deflection curves for the

Table 2
Mechanical properties of CP Ti (Grade 3) in the as-received (AR) condition and after hydrostatic extrusion. T indicates transverse section and L longitudinal section.

	$\sigma_{0.2}$ [MPa]	σ_{UTS} [MPa]	ε_u [%]	ε_f [%]
AR-T	396 ± 1	537 ± 12	4.43 ± 0.65	9.82 ± 0.75
AR-L	344 ± 14	494 ± 1	4.95 ± 0.63	8.97 ± 0.67
Extruded-T	562 ± 32	995 ± 7	2.65 ± 0.07	5.95 ± 0.07
Extruded-L	915 ± 70	970 ± 17	0.87 ± 0.16	3.06 ± 0.33

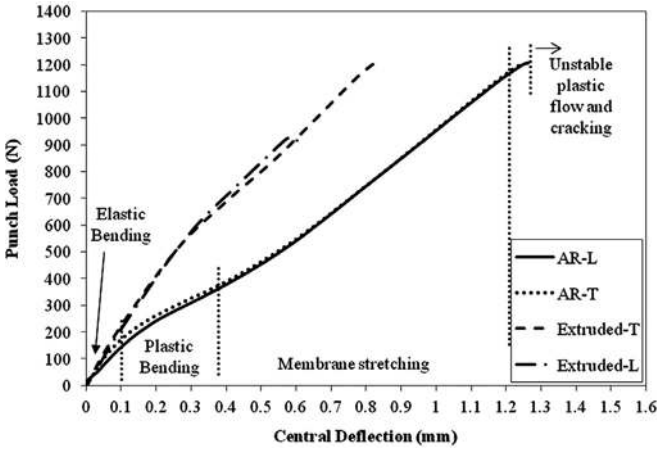

Fig. 8. Load–central deflection curves from small punch testing of CP Ti: as-received (AR) material and hydrostatically extruded material.

Table 3
Results of small punch testing.

Sample	F_{max} [N]	h_{max} [mm]	ε
AR-T	1243 ± 47	1.3 ± 0.05	0.32
AR-L	1213 ± 23	1.27 ± 0.05	0.30
Extruded-T	1163 ± 34	0.79 ± 0.03	0.12
Extruded-L	910 ± 59	0.60 ± 0.02	0.05

L- and T- small punch specimens nearly coincide and have the same maximum central deflection of ~1.3 mm (Fig. 8) and true uniform strain ε~0.3. Fig. 8 shows that hydrostatic extrusion results in a significant increase of the load required for deformation of small punch specimens to the same central deflection as well as to significant reduction of the maximum central deflection leading to the lower values of the true strain which can be induced in the specimens during small punch testing (Table 3). The hydrostatically extruded material shows anisotropy of bi-axial deformation behavior. First, the load-central deflection curves show higher load required for bi-axial deformation of the L-specimens in the membrane stretching regime (Fig. 8). Second, the L-specimens display lower maximum central deflection, ~0.6 mm, and lower value of true uniform strain, 0.12, compared to those for the T-specimens, ~0.8 mm and 0.05, respectively (Table 3).

Surface analysis of the small punch specimens tested up to cracking showed a significant anisotropy in failure behavior of the L- and T-extruded specimens. The T-specimens showed formation of cracks at φ~60° which are concentric to the dome as shown in Fig. 9a. These cracks were formed in symmetric manner with respect to the dome axis. Evidence of micro-shear band formation, with deformation bands having a length in the range of 5–15 μm, is observed in Fig. 9b. Two types of cracks were observed in the L-specimens: primary long cracks were formed along the extrusion direction at φ~50–60° and their further growth to the length of 200–400 μm was accompanied by formation of secondary cracks

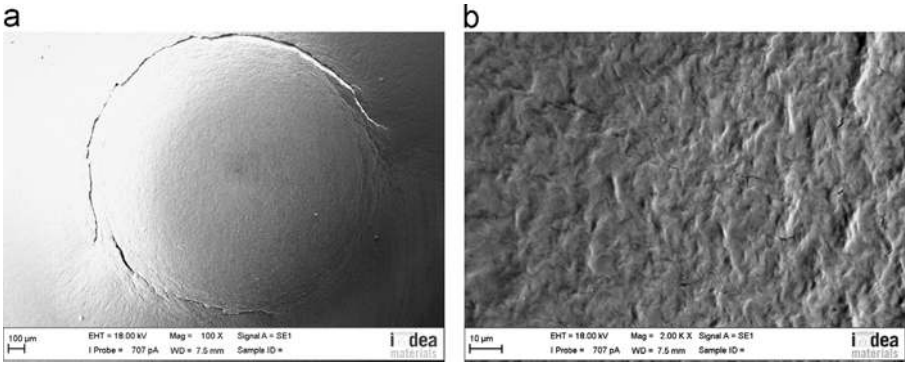

Fig. 9. SEM images of surface relief on the hydrostatically extruded T-specimen after small punch testing: (a) general view of the tested specimen and (b) at $\varphi \sim 30^{o}$.

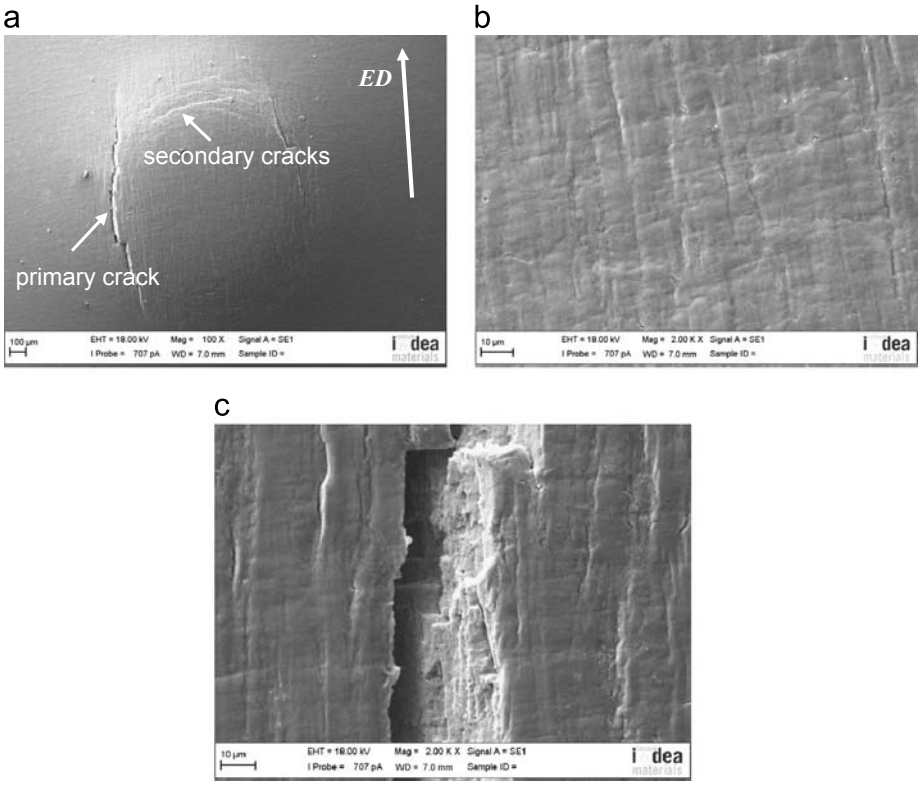

Fig. 10. SEM images of surface relief on hydrostatically extruded L-specimen after small punch testing: (a) general view of the tested specimen, (b) at $\varphi \sim 30^{\circ}$, (c) a primary crack at higher magnification.

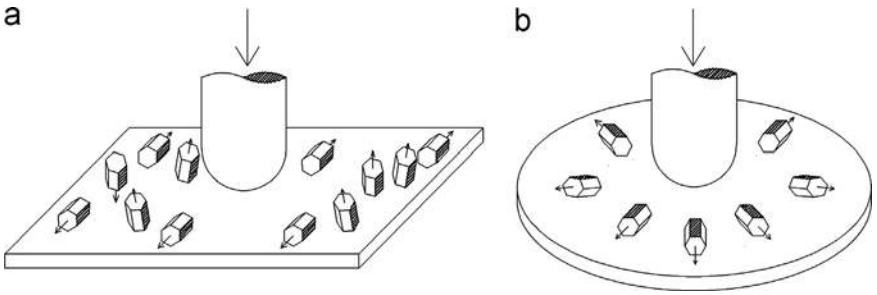

Fig. 11. Schematic drawings of crystallographic texture of extruded specimens during small punch testing: (a) L-specimen and (b) T-specimen.

perpendicular to the extrusion direction, as shown in Fig. 10. T h e anisotropy in bi-axial deformation and failure behavior of the hydrostatically extruded material can be related to (1) the lamellar-type microstructure and (2) the very strong crystallographic fiber texture developed during hydrostatic extrusion, though we suggest that the latter effect plays the major role. In the T-specimens, the *C*-axis and two prismatic planes of the hcp lattice are perpendicular and all basal planes are parallel to the punch axis (Fig. 11a), thus, resulting in homogeneous bi-axial plastic deformation in the area of bi-axial stretching followed by failure which is symmetrical with respect to the dome axis (Fig. 9a). In the L-specimens, the *C*-axis, basal planes, and prismatic planes are randomly inclined with

respect to the punch axis (Fig. 11b). Therefore, combinations of grains with various crystallographic orientations can be present in the microstructure of the L-specimens. Some combinations of soft grains and hard grains can lead to formation of the quazi-cleavage facets [43] which, in turn, can easily lead to their quick growth along lamellae boundaries since SPD processed Ti tends to show a low crack growth resistance [44].

5. Conclusions

1. Hydrostatic extrusion of CP Ti leads to the formation of ultrafine lamellar-type microstructure having a very strong crystallographic fiber texture with the *C*-axis perpendicular to the extrusion axis and $(10-10)$ direction parallel to the extrusion axis.
2. Hydrostatic extrusion of CP Ti leads to a significant increase of mechanical strength at the expense of ductility. There is a significant anisotropy of uni-axial tensile behavior of hydrostatically extruded CP Ti. The T-specimens show much lower yield strength but much higher strain hardening capacity compared to those of the L-specimens due to the strong crystallographic texture developed during hydrostatic extrusion.
3. There is anisotropy of bi-axial deformation behavior and failure of the hydrostatically extruded CP Ti during small punch testing. A higher load is required for bi-axial deformation of the L-specimens in the membrane stretching regime and the L-specimens show lower maximum central deflection and lower value of true uniform strain compared to those for the T-specimens. The T-specimens are deformed and fail in symmetric manner with respect to the punch axis whereas the failure of the L-specimens begins with formation of primary longitudinal cracks (parallel to the extrusion direction) and their growth followed by formation of secondary cracks (perpendicular to the extrusion direction). This anisotropy is related to the specific microstructure and texture developed in CP Ti during hydrostatic extrusion.

Acknowledgments

This work was carried out in frames of the European project LIMEDU (FP7 ERA-NET MATERA+ 2009, Project No MATERA/ESM-1889) funded by Fundacion MADRI+D and by the National Centre for Research and Development (Project NCBiR/ERA-NET MATERA+/03/2011). IS acknowledges gratefully the Spanish Ministry of Economy and Competitiveness for financial support through the Ramon y Cajal Fellowship. The authors thank the Laboratorio de Microscopía Electrónica de Transmisión (LABMET) for the TEM measurements.

References

[1] G. Lutjering, J.C. Williams, Titanium, Springer, Germany, 2003.
[2] D.M. Brunette, P. Tengvall, M. Textor, P. Thomsen, Titanium in Medicine, Springer, Germany, 2001.
[3] R.Z. Valiev, M.J. Zehetbauer, Y. Estrin, H.W. Hoeppel, Y. Ivanisenko, H. Hahn, G. Wilde, H.J. Roven, X. Sauvage, T.G. Langdon, Adv. Eng. Mater. 9 (2007) 527–533.
[4] Y.G. Ko, D.H. Shin, K.T. Park, C.S. Lee, Scr. Mater. 54 (2006) 1785–1789.
[5] D.H. Shin, I. Kim, J. Kim, Y.S. Kim, S.L. Semiatin, Acta Mater. 51 (2003) 983–996.
[6] J. Gubicza, Zs. Fogarassy, Gy. Krallics, J. Labar, T. Torkoly, Mater. Sci. Forum 589 (2008) 99–104.
[7] I. Sabirov, M.T. Perez-Prado, J.M. Molina-Aldareguia, I.P. Semenova, G.K. H. Salimgareeva, R.Z. Valiev, Scr. Mater. 64 (2011) 69–72.
[8] D.V. Gunderov, A.V. Polyakov, I.P. Semenova, G.I. Raab, A.A. Churakova, E. I. Gimaltdinova, I. Sabirov, J. Segurado, V.D. Sitdikov, I.V. Alexandrov, N. A. Enikeev, R.Z. Valiev, Mater. Sci. Eng. A 562 (2013) 128–136.
[9] A.V. Sergueeva, V.V. Stolyarov, R.Z. Valiev, A.K. Mukherjee, Scr. Mater. 45 (2001) 747–752.
[10] R.Z. Valiev, A.V. Sergueeva, A.K. Mukherjee, Scr. Mater. 49 (2003) 669–674.
[11] D.K. Yang, P.D. Hodgson, C.E. Wen, Scr. Mater. 63 (2010) 941–944.
[12] H.S. Kim, Mater. Sci. Eng. A 328 (2002) 317–323.
[13] H.S. Kim, S.J. Kim, J.W. Kim, D.H. Kim, W.J. Kim, Mater. Sci. Eng. A 528 (2011) 8479–8485.
[14] M. Lewandowska, K.J. Kurzydlowski, J. Mater. Sci. 43 (2008) 7299–7306.
[15] W. Pachla, M. Kulczyk, M. Sus-Ruszkowska, A. Mazur, K.J. Kurzydlowski, J. Mater. Process. Technol. 205 (2008) 173–182.
[16] K. Topolski, H. Garbacz, W. Pachla, K.J. Kurzydlowski, Phys. Status Solidi 7 (2010) 1391–1394.
[17] S. Zherebtsov, W. Lojkowski, A. Mazur, G. Salishchev, Mater. Sci. Eng. A 527 (2010) 5596–5603.
[18] K. Topolski, H. Garbacz, K.J. Kurzydlowski, Mater. Sci. Forum 584–586 (2008) 777–782.
[19] G.G. Yapici, I. Karaman, H.J. Maier, Mater. Sci. Eng. A 434 (2006) 294–302.
[20] R. Lapovok, P.D. Hodgson, J. Mech. Phys. Solids 57 (2009) 1851–1864.
[21] A. Taylor, M. Weiss, T. Hilditch, N. Stanford, P.D. Hodgson, Mater. Sci. Eng. A 555 (2012) 148–153.
[22] R. Yoda, K. Shibata, T. Morimitsu, D. Terada, N. Tsuji, Scr. Mater. 65 (2011) 175–178.
[23] E.C. Moreno-Valle, M.A. Monclus, J.M. Molina-Aldareguia, N. Enikeev, I. Sabirov, Metal. Mater. Trans. A 44 (2013) 2399–2408.
[24] ASTM B 348-09. Standard Specification for Titanium and Titanium Alloy Bars and Billets.
[25] W. Pachla, M. Kulczyk, A. Świderska-Środa, M. Lewandowska, H. Garbacz, A. Mazur, K.J. Kurzydłowski, Nanostructuring of metals by hydrostatic extrusion, in: Proceedings of the 9th International Conference on Mat. Forming ESAFORM-2006, Glasgow, UK, 26–28 April 2006, pp. 535–538.
[26] I. Alexander, S.S. Pavlov, M. Kiritani, Mater. Sci. Eng. A 350 (2003) 245–250.
[27] A. el-Domiaty, S.Z. Kassab, J. Mater. Process. Technol. 83 (1998) 72–83.
[28] J.M. Garcia-Infanta, A.P. Zhilyaev, A. Sharafutdinov, O.A. Ruano, F. Carreno., J. Alloys Compd. 473 (2009) 163–166.
[29] Z.X. Wang, H.J. Shi, J. Lu, P. Shi, X.F. Ma, Nucl. Eng. Des. 238 (2008) 3186–3193.
[30] Y.W. Ma, K.B. Yoon, Mater. Sci. Eng. A 527 (2010) 3630–3638.
[31] J.S. Ha, E. Fleury, Int. J. Pres. Ves. Pip. 75 (1998) 707–713.
[32] E. Fleury, J.S. Ha, Int. J. Pres. Ves. Pip. 75 (1998) 699–706.
[33] M.B. Toloczko, M.L. Hamilton, G.E. Lucas, J. Nucl. Mater. 283–287 (2000) 987–991.
[34] R.J. Contieri, M. Zanotello, R. Caram, Mater. Sci. Eng. A 527 (2010) 3994–4000.
[35] K. Hajizadeh, S. Ghobadi Alamdari, B. Eghbali, Physica B 417 (2013) 33–38
.[36] U.F Kocks, C.N. Tome, H.R. Wenk, Texture and Anisotropy, Cambridge University Press (2000) 203–207.
[37] S. Nemat-Nasser, W.G. Guo, J.Y. Cheng, Acta Mater. 47 (1999) 3705–3720.
[38] H. Conrad, Prog. Mater. Sci. 26 (1981) 123.
[39] M.M. Myshlyaev, S Yu, Mironov, Phys. Sol. State 44 (2002) 711–716.
[40] J. Gong, A.J. Wilkinson, Acta Mater. 57 (2009) 5693.
[41] G.E. Dieter, Mechanical Metallurgy, McGraw-Hill, Boston, MA, 1986.
[42] S.D. Norris, J.D. Parker, Mater. Sci. Technol. 12 (1996) 163–170.
[43] F.P.E. Dunne, D. Rugg, Fatigue Fract. Eng. Mater. Struct. 31 (2008) 949–958.
[44] I. Sabirov, R.Z. Valiev, I.P. Semenova, R. Pippan., Metal. Mater. Trans. A 41 (2010) 727–733.